

# **Numerical investigation of two-phase flows in highly-permeable porous media: Effect of the permeability on the drag force between fluid phases**

Maxime Cochenne, Hossein Davarzani, Yohan Davit

Ioannis Ignatiadis, Michel Quintard

May 20, 2020

The macroscopic description of two-phase flows in porous media requires accurate modelling of the drag forces between the two fluids and the solid phase. In standard porous media, where capillarity is often dominant, the fluids-solid interactions are well-known and the fluid-fluid drag force is neglected in the momentum transport equation. Two-phases flows in high permeability porous media, however, are often characterized by a larger area of the interface between the two fluids and the development of thin films. In such cases, the fluid-fluid interaction is not necessarily negligible and may play an important role in the momentum transport equations. Here, we use computational methods to study two-phase flows in a microfluidic device made of an array of cylinders squeezed between the two plates of a Hele-Shaw cell. The idea is to keep the geometry in the cell plane unmodified whereas the aperture  $h$  between the

plates is changed to explore different ranges of permeability. This is done by solving depth-averaged flow equations, taking advantage of the quasi-planar nature of the flow. We reproduce a film-flow regime and show that the fluid-fluid drag is non-negligible as it reaches between 5% and 60% of the solid-fluid drag. Furthermore, we find that the fluid-fluid drag increases as  $h^{-3}$  whereas the solid-fluids drag increases as  $h^{-2}$ . Our results demonstrate that the fluid-fluid drag force should not be neglected in momentum transport equations and behaves differently than the drag upon solids, confirming that a no-flow condition between fluids is not suitable. This is relevant for modelling macroscopic two-phase flows in microfluidic devices or highly permeable porous media, for which the film-flow regime is commonly encountered.

## 1. Introduction

An accurate description of two-phase flows in high-permeability porous media is of major importance in several practical applications. This includes soil remediation in sandy or gravely soils (Fetter et al., 2017), nuclear safety (Clavier et al., 2017) or catalytic fixed bed reactors (de Santos et al., 1991). However, most of the literature on two-phase flows in porous media is focused on low-permeability porous media.

For low-permeability porous media, surface tension forces often dominate the flow; thus the capillary, Bond, and Weber numbers are low. In this case, the fluid repartition is well described as two independent flow channels (Dullien, 2012; Blunt, 2017). The two fluids are segregated, the non-wetting fluid flowing into the larger pores whereas the wetting fluid occupies the smaller pores, and the area of the fluid-fluid interface is small (Fig. 1 (a)).

In contrast, for high-permeability porous media, the flow is the result of a complex interaction between capillary, gravity, viscous, and inertial forces (Davit and Quintard, 2018). Capillary effects no longer dominate and the capillary, Bond, and Weber numbers may be

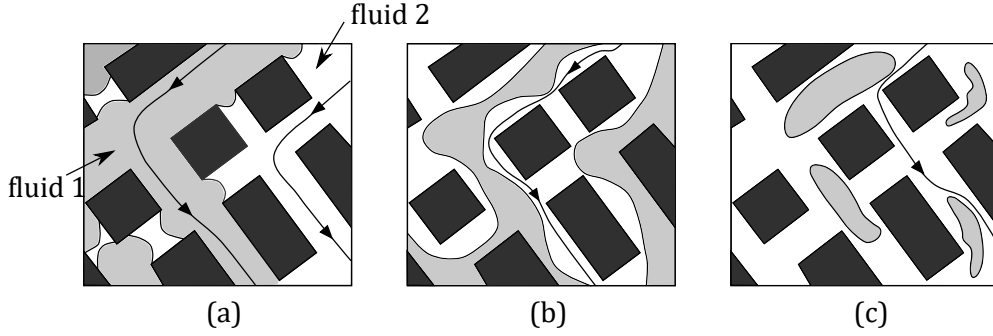


Figure 1: Illustration of possible fluids distributions in a 2D porous network with solid phase in black, the non-wetting fluid (fluid 1) in light grey, and the wetting fluid (fluid 2) in white, (a) the two fluids are flowing in different channels separated by numerous meniscus and the fluid-fluid interface extent is small, (b) the wetting and non-wetting fluids are flowing together in most of the pores as two continuous streams and (c) both fluids are flowing together in most of the pores and the non-wetting phase is discontinuous. - Adapted from (Dullien, 2012)

large. Schematically, the fluids distribution in the pore space take two forms. Either (i) the non-wetting fluid is continuous and flows in the center of the pores surrounded by the wetting fluid flowing as a thin film in contact with the solid (Fig. 1 (b)), or (ii) the non-wetting fluid is discontinuous and flows in the center of the pores in the form of droplets or ganglia (Fig. 1 (c)). In both cases, the surface area between the fluids is large and one would consider that the drag forces between the fluids are not negligible compared with the solid-fluids drag forces. This is in strong contrast with capillarity-dominated flow for which the area of the fluid-fluid interface is small. This is important because, as discussed in the following, modelling of these drag forces is the basis of any attempt to establish continuous relationships on a macroscopic scale starting from the pore scale. However, the fluid-fluid drag force terms are commonly overlooked in the traditional two-phases flow model in porous media, regardless of the medium's permeability (Dullien, 2012).

Indeed, the ubiquitous continuous model used to describe two-phase flows in porous media is based on a direct extension of Darcy's equations for one-phase flow (Wyckoff and Botset, 1936; Muskat, 1938). This heuristic generalization toward two-phase flows involves the introduction of the relative permeability terms which account only for the division of

the available void space between the fluids; thus each fluid phase acts as a supplementary solid regarding the other one and no interaction between the phases is taken into account (Dullien, 2012; Blunt, 2017). As a consequence, it is commonly assumed that the relative permeability depends (non-linearly) only on the saturation (Brooks and Corey, 1964; Van Genuchten, 1980). However, it has been shown that relative permeabilities also depend on the capillary number (Li et al., 2005), the flow regime (Avraam and Payatakes, 1995) or the viscosity ratio (Yuster et al., 1951; Ehrlich, 1993; Yiotis et al., 2007).

Since the early 1980s, numerous work aimed to improve the generalized Darcy equations on a sound physical basis. Among them, several authors used upscaling techniques (Marle, 1982; Auriault and Sanchez-Palencia, 1986; Whitaker, 1986; Lasseux et al., 1996). They found additional coupling permeability tensors that arise from taking the viscous terms at the fluid-fluid boundary condition into account during the upscaling. However, the importance of these coupling terms in the overall flow process has been a matter of debate (Ayub and Bentsen, 1999). Coupling terms have been shown to be of the same order as the dominant relative permeabilities in two-phase annular cocurrent flow in a cylindrical capillary tube for equal saturation (Yuster et al., 1951; Bacri et al., 1990). However it was pointed out that it is an idealized representation that greatly maximizes the extent of the interface surface between the fluids. Attempts to make the system more realistic, i.e., limit the extent of the interface between fluids, concluded that coupling terms should not be as important in real systems, considering that the extent of the interface surface the fluids is lower (Scott et al., 1953; Rakotomalala et al., 1995). Several authors directly measured the coupling permeability terms in natural media by performing steady-state cocurrent two-phase flows (Zarcone and Lenormand, 1994; Dullien and Dong, 1996; Ramakrishnan and Goode, 2015). Rose (1988) proposed to indirectly measure the coupling relative permeability terms by performing two different types of experiments. Several authors followed Rose's proposition and used cocurrent and countercurrent experiments (Bourbiaux et al., 1990; Bentsen and Manai, 1993). Each of these authors, except Zarcone and Lenormand, found that the cou-

pling relative permeabilities are significant. Recently, a whole model for each permeability term, including coupling ones, has been proposed for one-dimensional inertial two-phase flows in coarse non-consolidated porous media and further emphasizes the importance of coupling terms to correctly predict two-phase flows features in coarse porous media (Clavier et al., 2017). However, the experimental results suffer from two shortcomings. (i) It is impossible to know which type of flow regime dominates at the pore scale and thus the extent of the surface area between the fluids, and (ii) regarding indirect measurement, it was pointed out that the saturation between the two sets of experiments can strongly differ and therefore the measured relative permeabilities cannot be safely compared (Langaas and Papatzacos, 2001).

The use of micromodels overcomes the first problem, and they have been widely used to better understand two-phase flows in porous media (Karadimitriou and Hassanizadeh, 2012), and in particular for the study of transition between the flow regimes or appearance of displacement instabilities (Lenormand et al., 1988; Zhang et al., 2011). Such apparatus were employed to measure the relative coupling permeabilities for different flow regimes (Avraam and Payatakes, 1995) or study the impact of the fluid-fluid drag on the flow characteristics (Heshmati and Piri, 2018; Roman et al., 2019). Rothman (1990) performed numerical simulations in a 2D micromodel geometry and found that coupling permeabilities are comparable in magnitude with the case of the annular flow in a capillary tube. Fig. 2 shows Rothman's results along with some of the previously mentioned results on relative coupling permeabilities.

Hele-Shaw cells are one of the simplest example of micromodels as they consist of two parallel plates in between the fluids can flow. The great interest of such apparatus is that the equations governing the flows in Hele Shaw's cells are similar to Darcy's equation, and thus the permeability can be easily modified by increasing or decreasing the aperture between the plates (Saffman and Taylor, 1958). Recently, this characterisitc has been used to investigate the flow paths of a two-phases flow as a function of the micromodel thickness (Liu et al.,

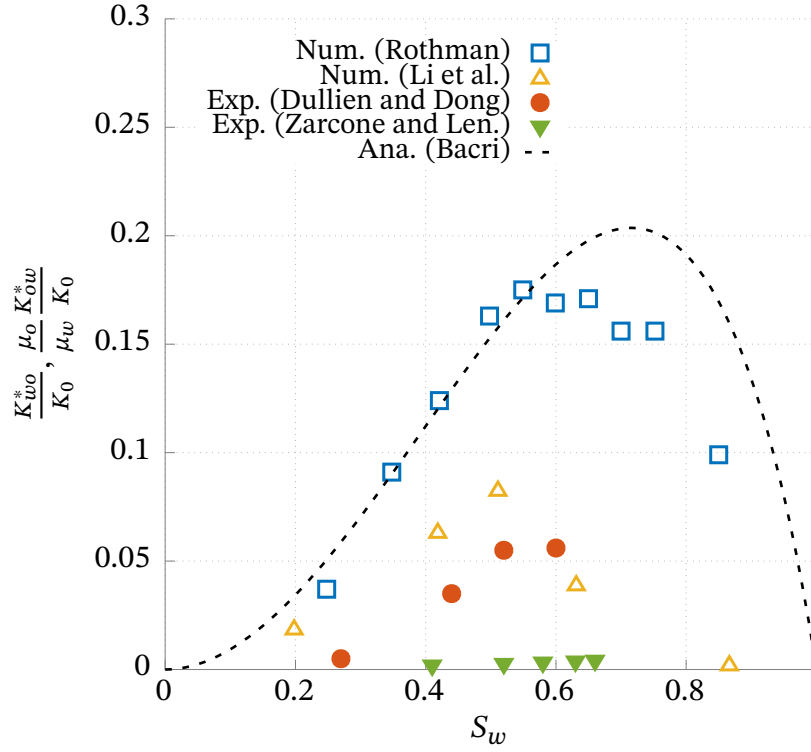


Figure 2: Normalized coupling relative permeabilities  $K_{ij}^*$  as a function of the wetting-fluid saturation  $S_w$  from experimental work (Dullien and Dong, 1996; Zarcone and Lenormand, 1994), numerical simulations (Rothman, 1990; Li et al., 2005) and analytical solution for a steady-state annular two-phase flow in a circular capillary tube (dashed line) (Bacri et al., 1990). The capillary theoretical case provides an upper limit in terms of permeability and extent of the interfacial surface area between the fluids.

2019) or to study the stability of an immiscible two-phases displacements in a Hele-Shaw cell with a spatially varying thickness (Jackson et al., 2017).

Here we present the influence of micromodel's intrinsic permeability and capillary number on the fluid-fluid drag and solid-fluids drag. The original idea of the article is to solve the appropriate depth-averaged equations for two-phase flows in a Hele-Shaw cell to study the effect of the varying intrinsic permeability on the drag forces without having to change the in-plane geometry.-

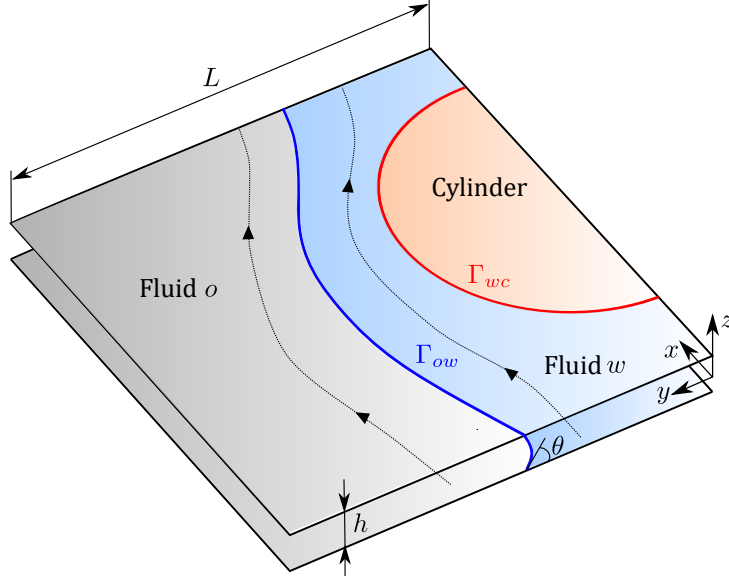


Figure 3: Schematic view of a cocurrent two-phase flow in a Hele-Shaw cell parallel to the  $x-y$  plane with a wedge of circular cross-section as a solid obstacle. The transverse dimension of the cell is noted  $L$  and  $h$  stands for the aperture between the plates. The boundary between the wetting-fluid  $w$  and the cylinder (in red) is noted  $\Gamma_{wc}$  and the boundary between the two fluids (in blue) is noted  $\Gamma_{ow}$ . No dynamic films along the plates are considered here and  $\theta$  stands for the non-zero contact angle between the two fluids and the plates.

## 2. Governing equations

In this section we derive the averaged flow equations for two-phases flows in a Hele-Shaw cell, starting from the three-dimensional Stokes equations. Then we proceed to the surface averaging of the resultant momentum equations to derive the unclosed form of the macroscopic momentum transport equations, which include all the drag force terms that we are interested in. The system under consideration is depicted in Fig. 3 which represents a quasi-planar cocurrent two-phase flow between two parallel plates with a wedge of circular cross-section as a solid obstacle. The transverse dimension of the cell is noted  $L$  and  $h$  is the length of the aperture between the plates.

**Depth-averaging** Three-dimensional continuity and Stokes equations for a Newtonian fluid in the absence of external forcing read, respectively,

$$\nabla \cdot \mathbf{u} = 0, \quad -\nabla p + \mu \nabla^2 \mathbf{u} = 0. \quad (1)$$

Since the length scales in the  $z$ -direction are smaller than the length scales in the  $x, y$  directions, an order of magnitude estimation allows to rewrite Eq. 1, at leading order, as

$$\nabla_{\parallel} \cdot \mathbf{u}_{\parallel} = 0, \quad \mu \frac{\partial^2 \mathbf{u}_{\parallel}}{\partial z^2} = \nabla_{\parallel} p(x, y), \quad (2)$$

where the subscript  $\mathbf{a}_{\parallel}$  stands for the components in the  $x$  and  $y$  directions of vector  $\mathbf{a}$ . One can write

$$\mathbf{u}_{\parallel}(x, y, z) = (\bar{u}(x, y)f(z), \bar{v}(x, y)f(z), 0)^T, \quad (3)$$

since the velocity variations in the  $x, y$  directions are much slower than the velocity variations in the  $z$ -direction. The depth-averaged velocity  $\bar{\mathbf{u}} = \frac{1}{h} \int_{-h/2}^{h/2} \mathbf{u}_{\parallel} dz$  is introduced and using its definition along with the no-slip boundary conditions at  $z \pm h/2$ , we obtain,

$$\mathbf{u}_{\parallel}(x, y, z) = \bar{\mathbf{u}}(x, y) \frac{3}{2} \left( 1 - 4 \frac{z^2}{h^2} \right). \quad (4)$$

Then, calculating the second derivative lead to,

$$\mu k^2 \bar{\mathbf{u}}(x, y) = -\nabla_{\parallel} p(x, y), \quad (5)$$

where  $k^2 = 12/h^2$  is a permeability term. Eq. 5 is valid in the limit of very small aspect ratio  $h/L$  and is analogous to the well known Darcy equation. To obtain a more versatile flow equation valid for moderate aspect ratio, we recognise that the velocity profile is described by a parabolic profile in the  $z$ -direction but we reintroduce the second derivatives along the



$x, y$  directions. Then, Eq. 1 read,

$$\nabla_{\parallel} \cdot \bar{\mathbf{u}} = 0, \quad \mu (\nabla_{\parallel}^2 \bar{\mathbf{u}} - k^2 \bar{\mathbf{u}}) = \nabla_{\parallel} p(x, y). \quad (6)$$

Eq. 6 are the continuity and momentum transport equations for the depth-averaged flow of one fluid. It has been shown that the velocity profile obtained for a flow in a channel with Eq. 6 lead to a reasonable approximation, up to aspect ratios  $h/L = 1$ , of the result obtained from the three-dimensional Stokes equations (Nagel and Gallaire, 2015). In the case of two-phase flows, these equations have to be written for each fluid and boundary conditions at the fluid-fluid interfaces are required. Continuity of the depth-averaged velocities across the interface and a jump of interface normal stress are sufficient if the surface tension is constant along the interface (Park and Homsy, 1984). These conditions are expressed

$$\bar{\mathbf{u}}_o - \bar{\mathbf{u}}_w = 0 \text{ at } \Gamma_{ow}, \quad (7)$$

$$(\bar{\sigma}_{\parallel w} - \bar{\sigma}_{\parallel o}) \cdot \mathbf{n}_{\parallel ow} = \gamma \left( \frac{\pi}{4} \kappa_{\parallel} + \frac{2}{h} \cos \theta \right) \mathbf{n}_{\parallel ow} \text{ at } \Gamma_{ow}, \quad (8)$$

where  $\bar{\sigma}_{\parallel i}$  is the in-plane stress tensor of fluid  $i$ ,  $\mathbf{n}_{\parallel ow}$  is the in-plane normal vector at the fluid interface pointing toward the fluid  $w$ ,  $\gamma$  is the surface tension,  $\kappa_{\parallel}$  is the in-plane interface curvature and  $\theta$  denotes the contact angle between the fluid interface and the plates (Fig. 3). The meniscus in the  $z$ -direction is approximated as a half-circle of radius  $h/2$  and the  $\pi/4$  correction for the in-plane curvature was derived by Park and Homsy (1984). In Eq. 8, we neglected the additional terms that pertain to the formation of the dynamic film (Park and Homsy, 1984) which scaled non-linearly with the capillary number. We rather considered a non-zero contact angle, and consequently, the absence of such thin films.

**Surface averaging** Here, we proceed to the spatial averaging of the in-plane momentum transport equations. We stop using the subscript  $\parallel$  in the following, since we work only with

depth-averaged or two-dimensional quantities. According to the volume averaging framework (Whitaker, 2013) and acknowledging that Eq. 6 are two-dimensional, the traditional averaging theorem for the depth-averaged quantity  $\bar{\omega}_i$  associated with the fluid  $i$  reads

$$\langle \nabla \bar{\omega}_i \rangle = \nabla \langle \bar{\omega}_i \rangle + \frac{1}{S} \int_{\Gamma_{ic}} \mathbf{n}_{ic} \bar{\omega}_i \, d\Gamma + \frac{1}{S} \int_{\Gamma_{ij}} \mathbf{n}_{ij} \bar{\omega}_i \, d\Gamma, \quad (9)$$

where,

$$\langle \bar{\omega}_i \rangle = \frac{1}{S} \int_{S_i} \bar{\omega}_i \, dS, \quad (10)$$

is the superficial surface average and  $S$  is the surface of a representative elementary cell. Applying the superficial surface average of Eq. 6 along with the averaging theorem and using traditional length-scale arguments (Whitaker, 2013) we obtain

$$\nabla \cdot \langle \bar{\mathbf{u}}_i \rangle = 0, \quad i, j = o, w, \quad i \neq j, \quad (11a)$$

$$\begin{aligned} & \frac{1}{S} \int_{\Gamma_{ic}} \mathbf{n}_{ic} \cdot \left( -p_i \mathbf{I} + \mu_i \left( \nabla \bar{\mathbf{u}}_i + (\nabla \bar{\mathbf{u}}_i)^T \right) \right) d\Gamma + \\ & + \frac{1}{S} \int_{\Gamma_{ij}} \mathbf{n}_{ij} \cdot \left( -p_i \mathbf{I} + \mu_i \left( \nabla \bar{\mathbf{u}}_i + (\nabla \bar{\mathbf{u}}_i)^T \right) \right) d\Gamma - \\ & - \mu_i k^2 \langle \bar{\mathbf{u}}_i \rangle = \varepsilon_i \nabla \langle p_i \rangle^i + \langle p_i \rangle^i \nabla \varepsilon_i, \quad i, j = o, w, \quad i \neq j, \end{aligned} \quad (11b)$$

where  $\mathbf{I}$  is the  $2 \times 2$  identity matrix and  $\langle p_i \rangle^i$  ( $\langle p_i \rangle^i = \langle p_i \rangle / \varepsilon_i$ ) is the intrinsic surface average pressure of fluid  $i$ , with  $\varepsilon_i$  the volume fraction of fluid  $i$ . The first integral is the drag force exerted upon the cylinders boundary by fluid  $i$  and the second integral pertains for the drag force exerted upon fluid  $j$  by fluid  $i$ . Two remarks must be made at this stage, firstly the presence of in-plane obstacle walls, depicted in Fig. 3 by a wedge of circular cross-section,

implies that the velocity field is three-dimensional near the obstacle because the flow is influenced by the no-flow condition over a distance of the order of the aperture  $h$  (Guyon et al., 1991). This also applies to the interface between fluids. A second point is that the integral on the fluid-fluid boundary interface is not strictly equivalent to an integral on this surface. Here, we consider that the contour in the  $x - y$  plane can be identically translated along the  $z$ -direction, which is an approximation since the meniscus is a half-circle for small  $h/L$  ratio. However, as shown in the Appendix A, using three-dimensional flow simulations in microchannels, these approximations remain reasonable.

If the variation of the saturation in space is negligible and acknowledging that, as illustrated in Fig. 3, only the wetting fluid  $w$  is in contact with the wedge, a more compact form of Eq. 11b reads

$$0 = -\varepsilon_w \nabla \langle p_w \rangle^w - \mu_w k^2 \langle \bar{\mathbf{u}}_w \rangle + \mathbf{d}_{wc} + \mathbf{d}_{wo}, \quad (12a)$$

$$0 = -\varepsilon_o \nabla \langle p_o \rangle^o - \mu_o k^2 \langle \bar{\mathbf{u}}_o \rangle + \mathbf{d}_{ow}, \quad (12b)$$

Here,  $\mathbf{d}_{ij}$  denotes the drag forces per unit surface area exerted upon phase  $j$  by phase  $i$  and which must be computed or modeled to obtain closed macroscopic equations. In the following, we are working on the direct calculation of the drag forces.

### 3. Direct numerical simulations

In this section, we introduce the standard Level Set method to capture the moving free interface between the fluids, along with the flow equations, both solved with the commercial Finite Element solver Comsol Multiphysics<sup>®</sup>.

#### 3.1. Equations

**Level Set model** The Level Set method is part of the Eulerian methods which have the particularity of easily handle the topological phases changes, in contrast to Lagrangian meth-

ods. As topological changes of the fluids are not excluded here, this motivated our choice for this method.

In the Level Set framework, the fluid phases are identified with a level set (scalar) function that goes smoothly from 0 to 1 across the fluid interface, which is implicitly defined as the iso-level  $\phi = 0.5$ . Transport of the level set function  $\phi$  is governed by

$$\frac{\partial \phi}{\partial t} + \nabla \cdot (\bar{\mathbf{u}}\phi) = \tau \nabla \cdot \left( \psi \nabla \phi - \phi(1 - \phi) \frac{\nabla \phi}{|\nabla \phi|} \right), \quad (13)$$

where  $\bar{\mathbf{u}}$  is the depth-averaged velocity field and  $\tau$  and  $\psi$  are two numerical parameters that control the diffuse interface thickness and the amount of initialization of  $\phi$  function, respectively (Olsson et al., 2007). We investigate the accuracy of the implicit definition of the interface as well as the effect of the value of the initialization parameter on the interface position in Appendix B. To do so we compare the Level-Set results with the results obtained with a Boundary Element Method code Nagel and Gallaire (2015).

**Flow equations** The governing flow equations are identical to the depth-averaged Eq. 6 except that one continuity and momentum transport equation is valid for the whole domain and thus contribution of capillary forces is included in the momentum transport equation,

$$0 = \nabla' \cdot \bar{\mathbf{u}} \quad (14a)$$

$$0 = -\nabla p + \mu(\phi) \left( \nabla^2 \bar{\mathbf{u}} - \frac{12}{h^2} \bar{\mathbf{u}} \right) + \gamma \left( \frac{\pi}{4} \nabla \cdot \left( \frac{\nabla \phi}{|\nabla \phi|} \right) - \frac{2}{h} \right) \delta(\phi) \mathbf{n}, \quad (14b)$$

where  $\delta$  is the Dirac delta function localized on the interface and  $\mathbf{n}$  denotes the unit normal to the interface, respectively defined as, bien.

$$\delta(\phi) = 6 |\nabla \phi| |\phi(1 + \phi)|, \quad \text{and} \quad \mathbf{n} = \frac{\nabla \phi}{|\nabla \phi|}. \quad (15)$$

We introduce the following reference and dimensionless quantities,

$$\bar{\mathbf{u}} = \bar{\mathbf{u}}' \times U_r, \quad p = p' \times \frac{\mu_r U_r}{L}, \quad \mathbf{x} = \mathbf{x}' \times L, \quad (16)$$

and the dimensionless continuity and momentum transport equations read,

$$0 = \nabla' \cdot \bar{\mathbf{u}}' \quad (17a)$$

$$0 = -\nabla' p' + \frac{\mu(\phi)}{\mu_r} \left( \nabla'^2 \bar{\mathbf{u}}' - \frac{12}{(h/L)^2} \bar{\mathbf{u}}' \right) + \frac{\gamma}{\mu_r U_r} \left( \frac{\pi}{4} \nabla' \cdot \left( \frac{\nabla' \phi}{|\nabla' \phi|} \right) - \frac{2}{h/L} \right) \delta'(\phi) \mathbf{n}, \quad (17b)$$

with  $\delta'(\phi) = 6 |\nabla' \phi| |\phi(1 + \phi)|$ . From Eq. 17b we note three dimensionless numbers, namely the viscosity ratio  $M(\phi) = \frac{\mu(\phi)}{\mu_r}$ , the capillary number  $Ca^{-1} = \frac{\gamma}{\mu_r U_r}$  and the aspect ratio  $h^* = h/L$ . For a small aspect ratio we can clearly see that the Darcean terms become preponderant.

**Geometry, boundary conditions and simulation parameters** Our macroscopic model resembling a Hele-Shaw cell with wedges of cylindrical cross-section confined between two plates as obstacles. This system is subdivided into five unit-cell (UC) subdomains encompassing one wedge, as depicted in Fig. 4. Taking advantage of the symmetry, we studied only the upper half of a row. Each fluid flows from left to right ( $x$ -direction) and the inlet boundary conditions for both fluids are a constant normal inlet velocity  $u_t^x$ . The outlet boundary condition for the flow is a reference pressure. The boundary conditions used are summarized in Tab.1. We choose the total inlet velocity as the reference velocity; thus the dimensionless inlet velocities can be expressed as a fractional flow  $f_f$ ,

$$f_f = \frac{u_w^x}{U_t}, \quad u_o^x = 1 - f_f, \quad \text{with} \quad U_t = u_w^x + u_o^x. \quad (18)$$

The non-wetting viscosity is taken as the reference viscosity and the respective value of each dimensionless parameters are inventoried in Tab. 2. The viscosity ratio is chosen in fa-

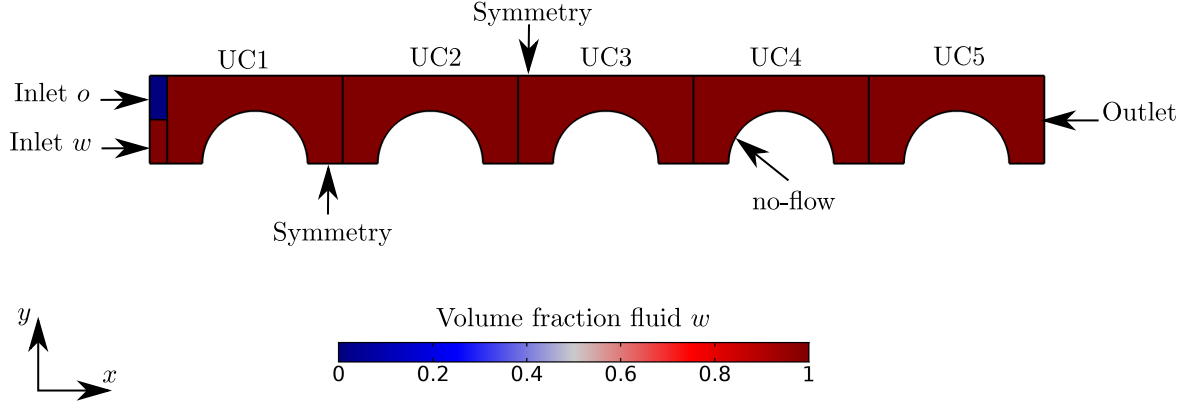


Figure 4: The geometry used is the superior half of an array of five cylindrical wedges inside five cuboids where both fluids are injected from left to right. Initially, the model is saturated with wetting fluid (red), and the width  $L$  of one Unit Cell (UC) is  $5 \times 10^{-4}$  m. Symmetry boundary conditions are used on both length sides and the no-flow boundary condition is imposed at the wedge boundary.

vor of the invading fluid to mimic the invasion of an initially fully water-saturated micro-model by an oil-like fluid. The initialization parameter in Eq. 13 is chosen in accordance with our findings in Appendix B, in which we show that the interface position is more accurate when the initialization parameter value is equal to the maximum inlet velocity value. We select a large range of plates aperture, however, the reader is warned that the depth-averaged equations derived in the previous section are outside their validity conditions for the extreme value  $h/L = 5$  (Nagel and Gallaire, 2015), on the other hand, it provides a limit 2-dimensionnal case. We conducted one-phase flow numerical simulations and found that the range of aperture corresponds to a range of intrinsic permeability between  $1.5 \times 10^4$  and 40 darcy. This is a range broad enough to investigate intrinsic permeability values typical of high-permeability porous media.

Table 1: Boundary conditions for flow variables and the Level Set function.

Boundary	$u$	$p$	$\phi$
Outlet	-	0	$\mathbf{n} \cdot \nabla \phi = 0$
Inlet $o$	$u_o^x$	-	0
Inlet $w$	$u_w^x$	-	1

Table 2: Simulation parameters.

Parameters	Value
$Ca = \frac{U_t \mu_o}{\gamma}$	from $7.5 \times 10^{-3}$ to 1
$M_w = \frac{\mu_w}{\mu_o}$	0.5
$f_f = \frac{u_w^x}{U_t}$	0.25
$h^* = h/L$	from 5 to $1/20$

**Mesh convergence study** Here we study the mesh convergence of the various drag forces. The dimensionless numbers for this study are  $Ca = 1$ ,  $h^* = 0.25$ ,  $f_f = 0.25$  and  $M_w = 0.5$ . We use a quadratic discretization for the velocity and the level-set function, and a linear discretization for the pressure. In Fig. 5 (a) the results are normalized with respect to the finer mesh result and are given as a function of the total number of mesh elements in the whole model. The fluid-fluid interface position for three different mesh densities is given in Fig. 5 (b). We obtain these results in the third unit-cell (UC3) at steady-state. The drag is not very sensitive to the mesh density and in particular the drag exerted upon the wedge. The difference between the intrinsic average pressures of the two fluids takes longer to converge with the mesh. The interface between the fluids is correct even for a coarse mesh and converges very quickly. In the following simulations, we used  $1 \times 10^5$  mesh elements in the whole domain.

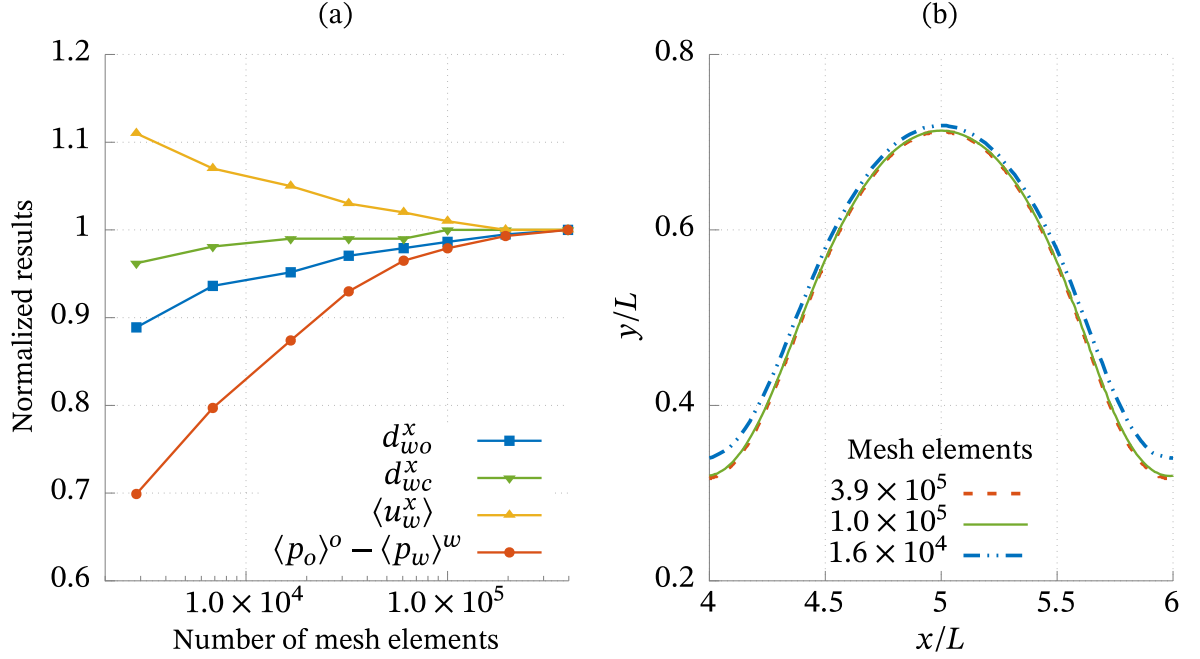


Figure 5: Mesh convergence study of (a) drag force ( $x$ -component) exerted upon the fluid-fluid boundary (blue), drag force ( $x$ -component) exerted upon the wedge (green), intrinsic average velocity of fluid  $w$  (yellow) and difference of the intrinsic average pressures (orange). All the results are normalized with respect to the result obtained with the finer mesh, at steady-state and in UC3. (b) Fluid-fluid interface position in UC3 at steady-state for different number of mesh elements in the whole geometry. The following results was obtained with a mesh of  $1 \times 10^5$  elements.

## 4. Results and discussion

Before we present the results for drag force terms, we briefly discuss the two-phase flow regime observed along with the variation of the saturation with time. The flow regime is an important concern since it drives the extent of the interfacial surface area between the fluids.

**Two-phase flow regimes** We observe that the two fluids remain continuous at all times and for the entire range of tested capillary numbers and dimensionless aperture. The interface between the fluids becomes stationary and a stationary state is reached for every



capillary number and dimensionless aperture values. Fig. 6 shows the initial, intermediate, and final configurations of the fluid repartition for the case  $Ca = 5 \times 10^{-2}$  and  $h^* = 0.25$ . At steady-state, the fluid-fluid interface is periodic on the three central unit cells whereas the interface is slightly deformed at the inlet and outlet cells, under the influence of boundary conditions.

Here we could have expected a break-up of the invading phase either by snap off phenomenon, or by the shear action of the wetting fluid flow. However, the channel at the pore throat is large and the fractional flow is low, which favours the continuity of the fluid phases. The flow-regime observed is a film-flow regime within the limit of the parameters chosen for this study. This flow-regime is favourable to the magnitude of the fluid-fluid drag terms, because the extent of the fluid-fluid interface is large and the interface is parallel to the dominant direction of the flow; thus it is subject to a high shear. In the following work, the results are obtained at steady-state and only in the central unit cell UC3 to be far from the perturbation caused by the inlet and outlet boundary conditions.

**Saturation** Wetting fluid saturation at steady-state decreases, in average, from 0.6 to 0.3 as the aperture between the plates decreases from 5 to  $1/20$ . This can be seen in Fig. 7, which present the saturation in UC3 as a function of the dimensionless aperture and for different capillary numbers. As the aperture between the plates increases, the fluid-fluid interface becomes flatter but the film thickness at the throat pore level barely changes, therefore, the saturation of the wetting fluid increases. This is noticeable in the embedded saturation fields in Fig. 7. Increasing capillary number decreases slightly the wetting fluid saturation, but with a more limited effect than the aperture variation.

**Drag force** We compute the fluid-fluid according to Eq.11b. The viscous part is obtained through the velocity gradient available at the  $\phi = 0.5$ -contour and the pressure part is obtained by application of the divergence theorem (Appendix C). The drag force exerted upon the wedge boundary is computed straight forward from the model. In the following, we

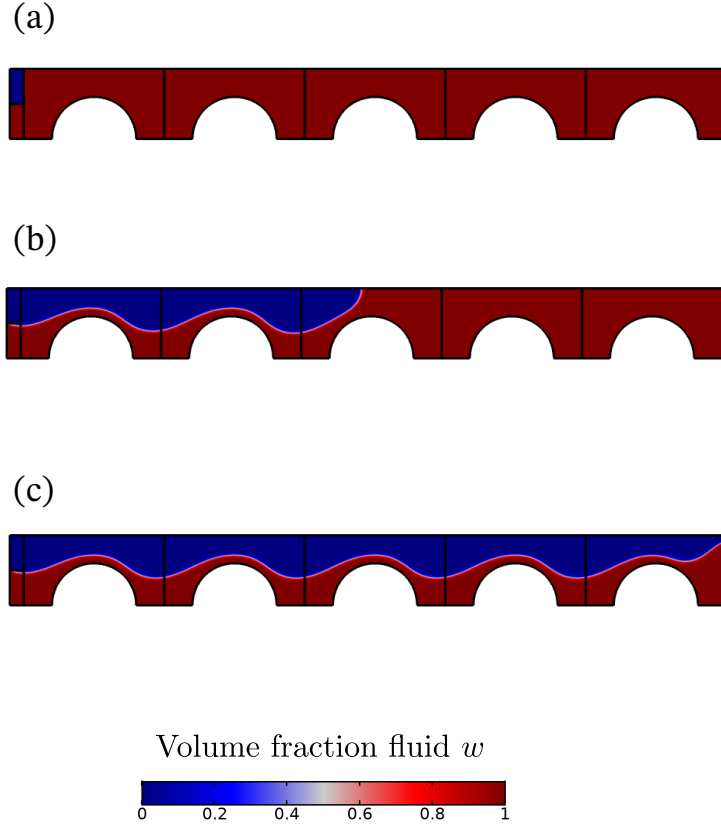


Figure 6: Fluids repartition along the superior half-row at (a) the initial time, (b) for an intermediate time and (c) final time (steady-state reached) for  $Ca = 0.05$ ,  $f_f = 0.25$ ,  $M_w = 0.5$  and  $h^* = 0.25$ . At steady-state the fluid-fluid interface taken on the central unit cells is periodic whereas it is slightly deformed in the first and last UC under the influence of the boundary conditions.

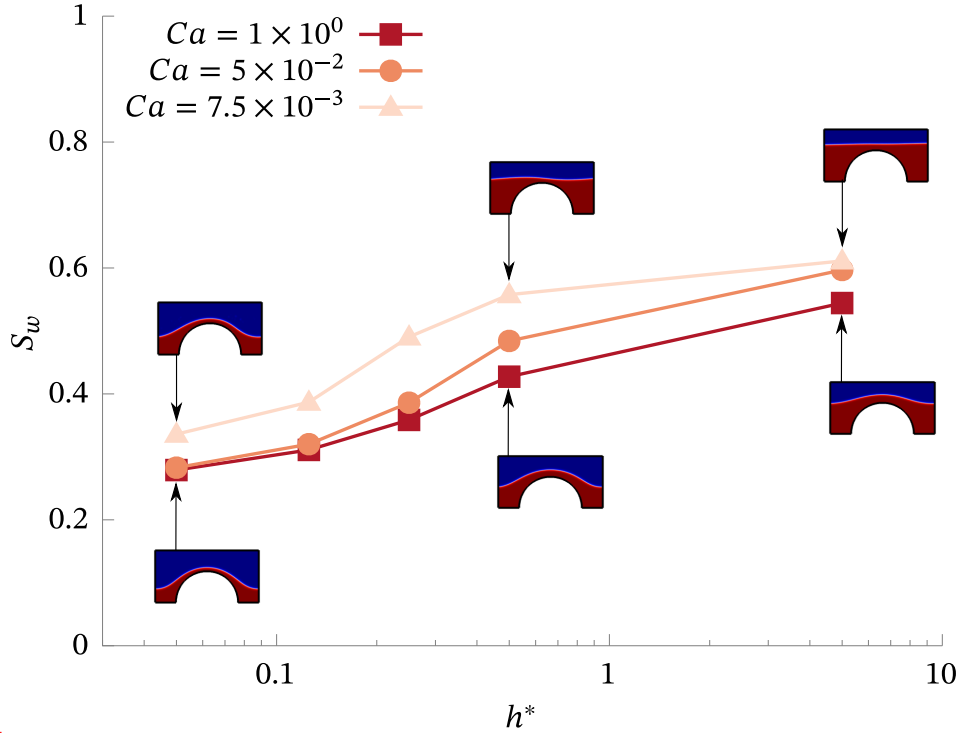


Figure 7: Fluid saturation at steady-state in UC3 as a function of the dimensionless aperture and for different capillary numbers. Fields of the level-set function at steady-state in UC3 are given for the selected value of the dimensionless aperture and  $Ca = 1$  and  $Ca = 7.5 \times 10^{-3}$ . As the aperture increases the interface flattens and the wetting fluid saturation increases. A decrease in the capillary number acts in the same way, albeit less strongly. -

are interested in the drag force component in the  $x$ -direction, i.e., the main flow direction. The total drag force ( $x$ -component) exerted upon the solid-fluids boundaries, denoted  $d_s^x$ , is the sum of the drag upon the wedge and upon the cell plates by both fluids. The total fluid-fluid drag, denoted  $d_f^x$ , is the sum of the contribution of each fluid, i.e.,  $d_f^x = d_{ow}^x + d_{wo}^x$ . In the following, the  $x$ -component of the drag forces are expressed per unit surface area of unit-cell.

The total drag exerted upon the fluid-fluid interface reaches between 5 and 58.69% of the total drag exerted upon the solid-fluids boundaries. This is shown in Fig. 8, on which we plot the ratio  $d_f^x/d_s^x$  as a function of the dimensionless aperture between the cell plates for different capillary numbers. The main observation here is that the fluid-fluid drag interface is not negligible compared to the solid-fluids drag. It is interesting to note that for  $h^* < 0.5$ , the part of the fluid-fluid drag decreases, compared with the solid-fluids drag, as the aperture between the plates increases. Furthermore, the smaller the capillary number, the smaller the fluid-fluid drag compared to the solid-fluids drag for an increasing aperture. At first glance, this may seem contradictory, since enlarging the aperture decreases the fluid's friction upon the plates.

One can better understand the above mentioned behavior with Fig. 9, which present the total drag upon either the solid-fluid interface or the fluid-fluid interface as a function of the dimensionless aperture. The drag forces at the fluid-fluid and solid-fluid interfaces logically increase as the capillary number increases. In the same way, the fluid-solid drag increases as the aperture between the plates decreases. Regarding the higher capillary number,  $Ca = 1$ , both  $d_s^x$  and  $d_f^x$  evolve as  $h^{-2}$ . However, for smaller capillary numbers, the fluid-fluid drag scales as  $h^{-3}$  whereas the solid-fluids drag upon the interface remains the same with a  $h^{-2}$  behaviour. This explains the influence of the capillary number and the origin of the variation in the  $d_f^x/d_s^x$  ratio. We add that  $d_s^x$  is not entirely driven by the fluid friction upon the plates, as might be suggested by the  $h^{-2}$  behavior. In fact, the drag force upon the wedge is at least about 80% of the drag upon the plates, for  $h^* = 1/20$ .

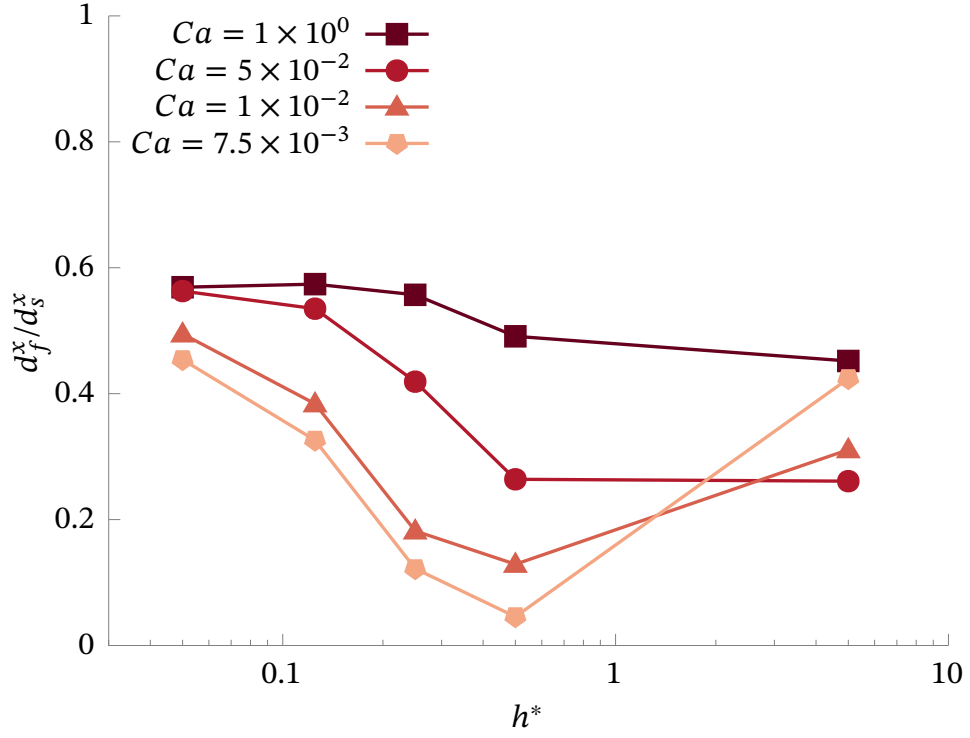


Figure 8: Ratio of the total drag force ( $x$ -component) exerted upon the fluid-fluid interface over the total drag force ( $x$ -component) exerted upon the fluid-solid interface as a function of the dimensionless aperture and for different capillary numbers (in UC3 for  $f_f = 0.25$  and  $M_w = 0.5$ ).

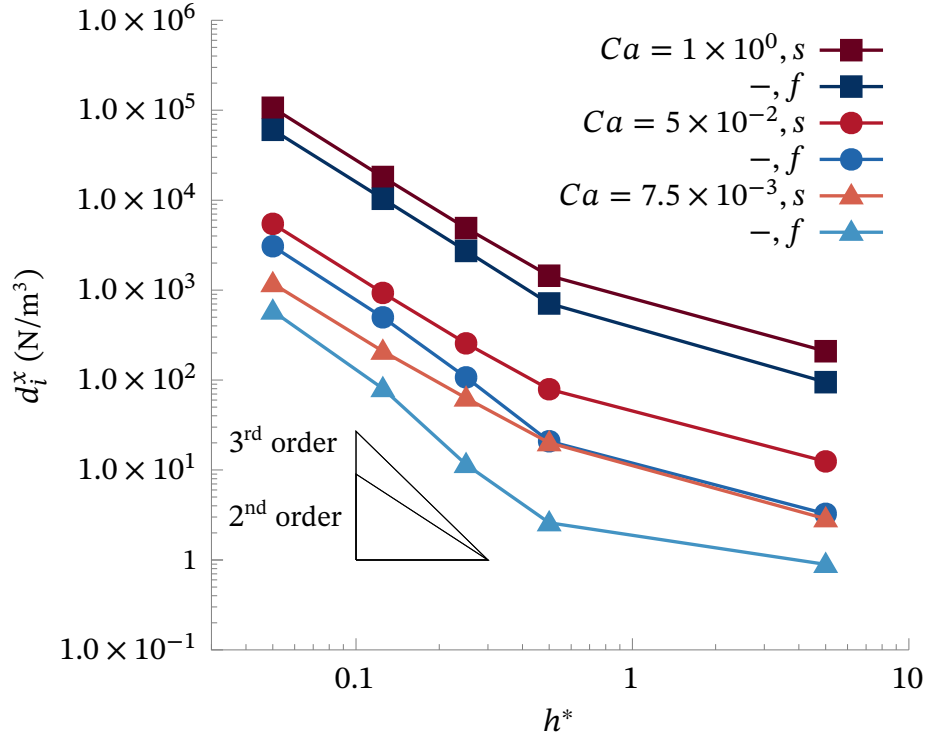


Figure 9: Total solid-fluid drag force and total fluid-fluid drag force as a function of the dimensionless aperture and for different capillary numbers (in UC3 for  $f_f = 0.25$  and  $M_w = 0.5$ ). Fluid-fluid drag increases more than the solid-fluid drag as the aperture decreases.

We present on Fig. 10 the viscous and pressure parts of the fluid-fluid drag force. For dimensionless aperture lower than  $1/2$ , the viscous part is negligible compared with the pressure part; thus, the pressure drives the  $h^{-2}$  and  $h^{-3}$  behaviors, depending on the capillary number. As the plates aperture decreases, for a constant inlet velocity and a constant output pressure boundary condition; the pressure gradient through the micromodel increases, and the pressure force exerted by the flow on the solid-fluid and fluid-fluid interfaces as well. One can look at the pressure fields in UC3 at steady-state for different capillary numbers and different apertures to better understand the effect of capillary number on pressure. As shown in Fig. 11, regarding  $Ca = 1$ , the pressure gradient along the  $x$ -direction across the cell is multiplied by 100 as the opening between the plates divided by ten, following Equation (5). However, for  $Ca = 0.01$ , and for the same change of plates aperture, the pressure gradient across the cell is multiplied by 2,000. A noteworthy feature of the pressure gradient is how it compares with the pressure jump across the fluid-fluid interface because of the interface curvature. Indeed, for  $Ca = 1$ , the pressure jump and the pressure gradient are about the same order when  $h^* = 0.5$ , but the former becomes negligible in front of the latter as the opening decreases. This is to be expected since the pressure gradient increases as  $h^{-2}$ , whereas the pressure jump increases as  $h^{-1}$  provided that it is mainly induced by the curvature of the fluid interface in the  $z$ -direction.-

We verify this last statement by looking at Fig. 12 which show the difference between the dimensionless mean intrinsic pressures of the fluids as a function of the aperture, along with the pressure jump produced by the curvature in the  $z$ -direction. There is a very slight discrepancy between the two quantities for  $Ca = 1$ , but it is clear that the pressure jump due to the interface curvature in the  $z$ -direction produces the difference between the average intrinsic pressures, regardless of the capillary number tested here.

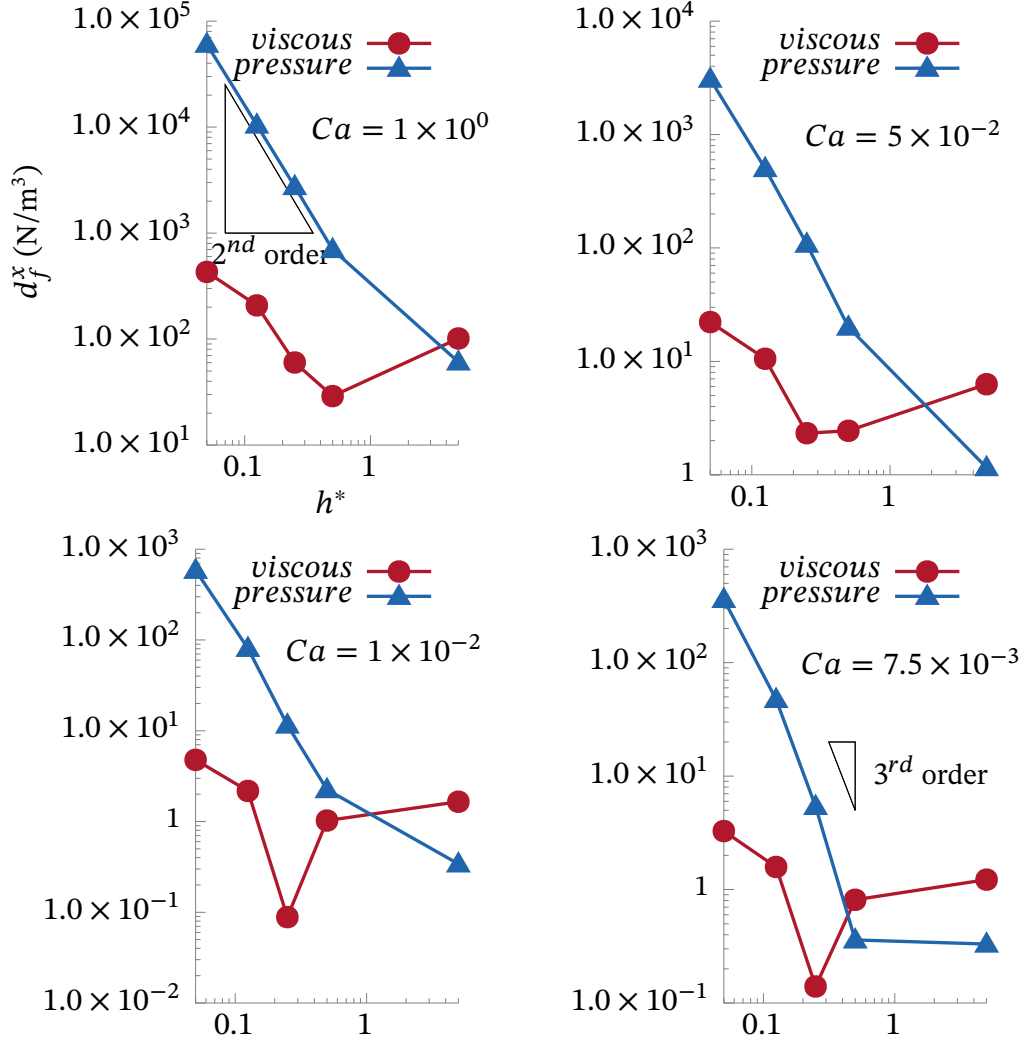


Figure 10: Pressure and viscous part of the total fluid-fluid drag force as a function of the dimensionless aperture and for different values of the capillary number (in UC3 for  $f_f = 0.25$  and  $M_w = 0.5$ ). The pressure part of the drag drives the  $h^{-2}$  and  $h^{-3}$  behaviors.



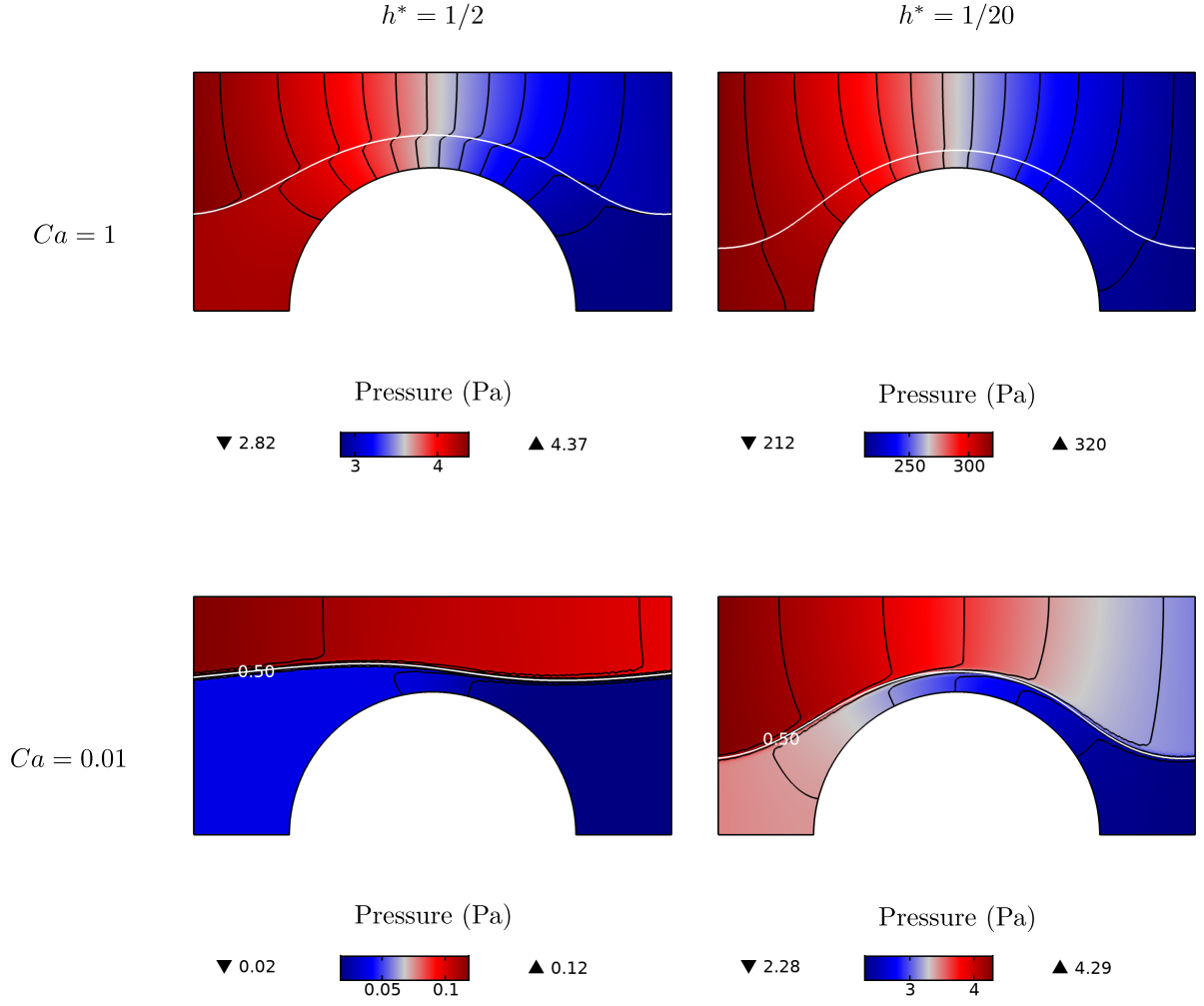


Figure 11: Pressure fields in UC3 at steady-state for  $Ca = 1$  and  $Ca = 0.01$  and dimensionless aperture values  $h^* = 0.5$  and  $h^* = 0.05$ . Isobar are represented in solid black lines and the solid white lines stand for the fluid-fluid interface defined by the  $\phi = 0.5$  contour (in UC3 for  $f_f = 0.25$  and  $M_w = 0.5$ ). The pressure jump across the interface is large compared to the pressure gradient across the cell for  $Ca = 0.01$  and  $h^* = 0.5$ , whereas it is the contrary for  $Ca = 1$  and  $h^* = 1/20$ .

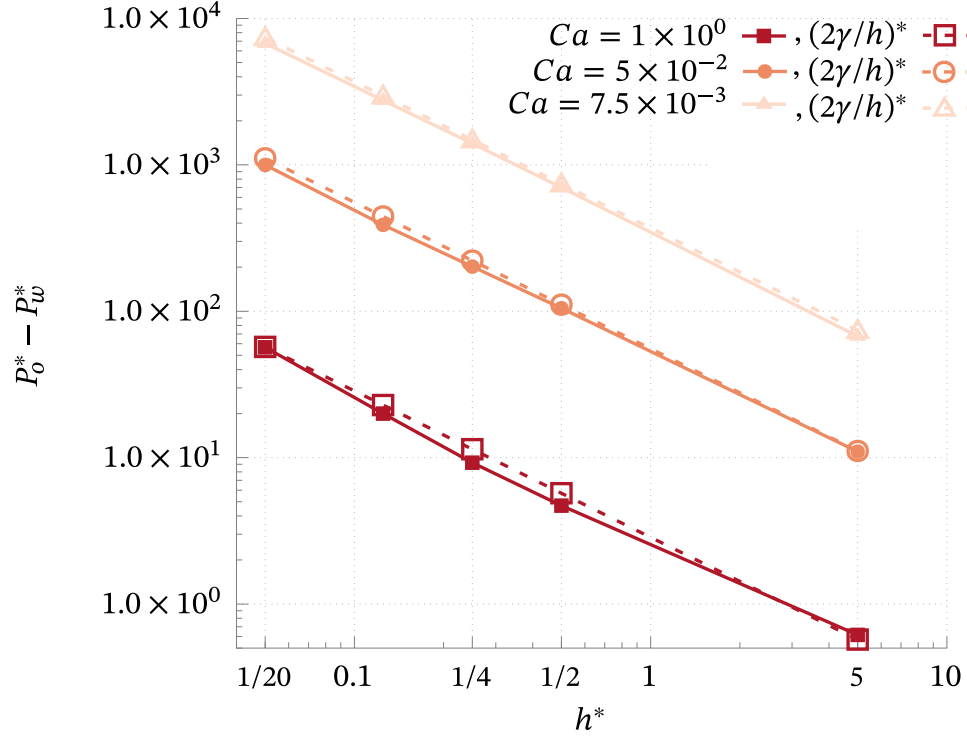


Figure 12: Dynamic pressure difference and pressure jump due to the interface curvature in the  $z$ -direction  $(2\gamma/h)$  normalized with respect to the reference pressure  $(U_T\mu_o/L)$  as a function of the dimensionless aperture and for different capillary numbers (in UC3 for  $f_f = 0.25$  and  $M_w = 0.5$ ). The difference  $P_o - P_w$  is positive and entirely induced by the pressure jump due to the out-of-plane meniscus.

## 5. Conclusion

In this study we conducted direct simulations of depth-averaged two-phases flows, and we investigated the effect of the permeability on the drag forces exerted upon the different phase interfaces. The permeability was changed by varying the Darcean term which arising from the depth-averaging, thus without altering the in-plane geometry. These drag terms have to be modelled to obtain the macroscopic momentum transport equations but the drag exerted upon the the fluid-fluid interface is commonly neglected for flow driven by capillarity forces. Here we focused on film-flow regime pourencountered in two-phases flows in high permeability porous media or in microfluidic devices. We found that the drag exerted upon the fluid-fluid interface should not be neglected into the momentum transport equations for film-flow regimes. Lower permeability does not make the drag force terms at the interface negligible as long as the flow regime remains a film regime. On the contrary, the fluid-fluid drag force increases faster than the drag upon the fluid-solid interfaces, as the aperture between the plates decreases.

## References

- Auriault, J., Sanchez-Palencia, E., 1986. Remarques sur la loi de darcy pour les écoulements biphasiques en milieu poreux. *Journal of Theoretical and Applied Mechanics*, Numéro Spécial , p141–156.
- Avraam, D.G., Payatakes, A.C., 1995. Generalized relative permeability coefficients during steady-state two-phase flow in porous media, and correlation with the flow mechanisms. *Transport in Porous Media* 20, 135–168. doi:10.1007/bf00616928.
- Ayub, M., Bentsen, R.G., 1999. Interfacial viscous coupling: a myth or reality? *Journal of Petroleum Science and Engineering* 23, 13–26.
- Bacri, J.C., Chaouche, M., Salin, D., 1990. Modèle simple de perméabilités relatives croisées. *Comptes rendus de l'Académie des sciences. Série 2, Mécanique, Physique, Chimie, Sciences de l'univers, Sciences de la Terre* 311, 591–597.
- Bentsen, R.G., Manai, A.A., 1993. On the use of conventional cocurrent and countercurrent effective permeabilities to estimate the four generalized permeability coefficients which arise in coupled, two-phase flow. *Transport in Porous Media* 11, 243–262.
- Blunt, M.J., 2017. *Multiphase flow in permeable media: A pore-scale perspective*. Cambridge University Press.
- Bourbiaux, B.J., Kalaydjian, F.J., et al., 1990. Experimental study of cocurrent and countercurrent flows in natural porous media. *SPE Reservoir Engineering* 5, 361–368.
- Brooks, R., Corey, T., 1964. Hydraulic properties of porous media. *Hydrology Papers*, Colorado State University 24, 37.
- Clavier, R., Chikhi, N., Fichot, F., Quintard, M., 2017. Modeling of inertial multi-phase flows through high permeability porous media: Friction closure laws. *International Journal of Multiphase Flow* 91, 243–261.

- Davit, Y., Quintard, M., 2018. One-phase and two-phase flow in highly permeable porous media. *Heat Transfer Engineering* , 1–19.
- Dullien, F.A.L., 2012. Porous media: fluid transport and pore structure. Academic press.
- Dullien, F.A.L., Dong, M., 1996. Experimental determination of the flow transport coefficients in the coupled equations of two-phase flow in porous media. *Transport in Porous Media* 25, 97–120. doi:10.1007/bf00141264.
- Ehrlich, R., 1993. Viscous coupling in two-phase flow in porous media and its effect on relative permeabilities@bookbear2013dynamics, title=Dynamics of fluids in porous media, author=Bear, Jacob, year=2013, publisher=Courier Corporation . *Transport in Porous Media* 11, 201–218.
- Fetter, C.W., Boving, T., Kreamer, D., 2017. Contaminant hydrogeology. Waveland Press.
- Guyon, E., Petit, L., Hulin, J.P., 1991. Hydrodynamique physique. interéditions.
- Heshmati, M., Piri, M., 2018. Interfacial boundary conditions and residual trapping: A pore-scale investigation of the effects of wetting phase flow rate and viscosity using micro-particle image velocimetry. *Fuel* 224, 560 – 578. URL: <http://www.sciencedirect.com/science/article/pii/S0016236118303971>, doi:<https://doi.org/10.1016/j.fuel.2018.03.010>.
- Jackson, S., Power, H., Giddings, D., Stevens, D., 2017. The stability of immiscible viscous fingering in hele-shaw cells with spatially varying permeability. *Computer Methods in Applied Mechanics and Engineering* 320, 606–632.
- Karadimitriou, N., Hassanizadeh, S., 2012. A review of micromodels and their use in two-phase flow studies. *Vadose Zone Journal* 11.
- Langaas, K., Papatzacos, P., 2001. Numerical investigations of the steady state relative permeability of a simplified porous medium. *Transport in Porous Media* 45, 241–266.

- Lasseux, D., Quintard, M., Whitaker, S., 1996. Determination of permeability tensors for two-phase flow in homogeneous porous media: theory. *Transport in Porous Media* 24, 107–137.
- Lenormand, R., Touboul, E., Zarcone, C., 1988. Numerical models and experiments on immiscible displacements in porous media. *Journal of fluid mechanics* 189, 165–187.
- Li, H., Pan, C., Miller, C.T., 2005. Pore-scale investigation of viscous coupling effects for two-phase flow in porous media. *Physical Review E* 72. doi:10.1103/physreve.72.026705.
- Liu, J., Ju, Y., Zhang, Y., Gong, W., 2019. preferential paths of air-water two-phase flow in porous structures with special consideration of channel thickness effects. *Scientific reports* 9, 1–13.
- Marle, C.M., 1982. On macroscopic equations governing multiphase flow with diffusion and chemical reactions in porous media. *International Journal of Engineering Science* 20, 643 – 662. doi:[https://doi.org/10.1016/0020-7225\(82\)90118-5](https://doi.org/10.1016/0020-7225(82)90118-5).
- Muskat, M., 1938. The flow of homogeneous fluids through porous media. *Soil Science* 46, 169.
- Nagel, M., Gallaire, F., 2015. Boundary elements method for microfluidic two-phase flows in shallow channels. *Computers & Fluids* 107, 272–284.
- Olsson, E., Kreiss, G., Zahedi, S., 2007. A conservative level set method for two phase flow ii. *Journal of Computational Physics* 225, 785 – 807. doi:<https://doi.org/10.1016/j.jcp.2006.12.027>.
- Park, C.W., Homsy, G., 1984. Two-phase displacement in hele shaw cells: theory. *Journal of Fluid Mechanics* 139, 291–308.
- Rakotomalala, N., Salin, D., Yortsos, Y.C., 1995. Viscous coupling in a model porous medium geometry: Effect of fluid contact area. *Applied scientific research* 55, 155–169.

- Ramakrishnan, T.S., Goode, P.A., 2015. Measurement of off-diagonal transport coefficients in two-phase flow in porous media. *Journal of colloid and interface science* 449, 392–398.
- Roman, S., Soullaine, C., Kovscek, A.R., 2019. Pore-scale visualization and characterization of viscous dissipation in porous media. *Journal of Colloid and Interface Science* doi:<https://doi.org/10.1016/j.jcis.2019.09.072>.
- Rose, W., 1988. Measuring transport coefficients necessary for the description of coupled two-phase flow of immiscible fluids in porous media. *Transport in Porous Media* 3, 163–171. URL: <https://doi.org/10.1007/BF00820343>, doi:10.1007/BF00820343.
- Rothman, D.H., 1990. Macroscopic laws for immiscible two-phase flow in porous media: Results from numerical experiments. *Journal of Geophysical Research* 95, 8663. doi:10.1029/jb095ib06p08663.
- Saffman, P.G., Taylor, G.I., 1958. The penetration of a fluid into a porous medium or heleshaw cell containing a more viscous liquid. *Proceedings of the Royal Society of London. Series A. Mathematical and Physical Sciences* 245, 312–329.
- de Santos, J.M., Melli, T.R., Scriven, L.E., 1991. Mechanics of gas-liquid flow in packed-bed contactors. *Annual Review of Fluid Mechanics* 23, 233–260. doi:10.1146/annurev.fl.23.010191.001313.
- Scott, P., Rose, W., et al., 1953. An explanation of the yuster effect. *Journal of Petroleum Technology* 5, 19–20.
- Van Genuchten, M.T., 1980. A closed-form equation for predicting the hydraulic conductivity of unsaturated soils 1. *Soil science society of America journal* 44, 892–898.
- Whitaker, S., 1986. Flow in porous media II: The governing equations for immiscible, two-phase flow. *Transport in porous media* 1, 105–125.

- Whitaker, S., 2013. The method of volume averaging. volume 13. Springer Science & Business Media.
- Wyckoff, R.D., Botset, H.G., 1936. The flow of gas-liquid mixtures through unconsolidated sands. *Physics* 7, 325–345.
- Yiotis, A.G., Psihogios, J., Kainourgiakis, M.E., Papaioannou, A., Stubos, A.K., 2007. A lattice boltzmann study of viscous coupling effects in immiscible two-phase flow in porous media. *Colloids and Surfaces A: Physicochemical and Engineering Aspects* 300, 35 – 49. doi:<https://doi.org/10.1016/j.colsurfa.2006.12.045>. proceedings of the Fourth International TRI/Princeton Workshop.
- Yuster, S., et al., 1951. Theoretical considerations of multiphase flow in idealized capillary systems, in: *Proceedings of the Third World Petroleum Congress*, E. Brill The Hague. pp. 437–445.
- Zarcone, C., Lenormand, R., 1994. Détermination expérimentale du couplage visqueux dans les écoulements diphasiques en milieu poreux. *Comptes rendus de l'Académie des sciences. Série II, Mécanique, physique, chimie, astronomie* 318, 1429–1435.
- Zhang, C., Oostrom, M., Wietsma, T.W., Grate, J.W., Warner, M.G., 2011. Influence of viscous and capillary forces on immiscible fluid displacement: Pore-scale experimental study in a water-wet micromodel demonstrating viscous and capillary fingering. *Energy & Fuels* 25, 3493–3505.



## A. Approximation made on the drag force when considering a fluid-fluid flat interface

We conduct three-dimensional one-phase flow simulations into a microchannel to determine the approximation made on the drag calculation when considering that the fluid-fluid contour can be translated along the  $z$ -direction.

One side of the microchannel is a half-circle wall to mimic a fluid-fluid interface whereas the opposite side is a flat wall (Fig. 13). We obtain the curved side by extruding a cylinder; thus a special treatment is done to correctly meshed the very thin part left, and we build very small chamfers (Fig. 13). We compute the drag force per unit surface area on each sidewall of the microchannel and plot in Fig. 14 the drag force exerted upon the curved side normalized with respect to the flat wall. The drag per unit surface area exerted upon the curved wall is roughly 70% of the drag per unit surface area upon the flat wall. Giving the greater extent of surface area for the curved wall, the difference regarding the drag value is negligible.

## B. Comparison with a Boundary Element Method

Here we validate the Level Set (LS) code by comparison with a Boundary-Element Method (BEM) (Nagel and Gallaire, 2015), which relies on a surface discretization of the interface and a pseudo-analytical formulation in the bulk of the phases. This allows us to precisely locate the interface, even in the case of very thin film flow, and to carefully analyze the choice of parameters in Eq. 13.

The test case resembles the case study (Fig. 15). The model is initially fully saturated with fluid  $w$ , with the exception of the channel through which fluid  $o$  is injected. We test either the  $\phi = 0.5$  contour is an appropriate definition for the fluid-fluid interface and in what extent the value of the initialization parameter  $\psi$  can change the interface position. In Fig. 16 we present the half-part of the model and the interface between the fluids at time  $t = 2.5$ , for an aspect ratio  $h/L$ , where  $L$  is the width of the fluid  $o$  inlet channel. We present three

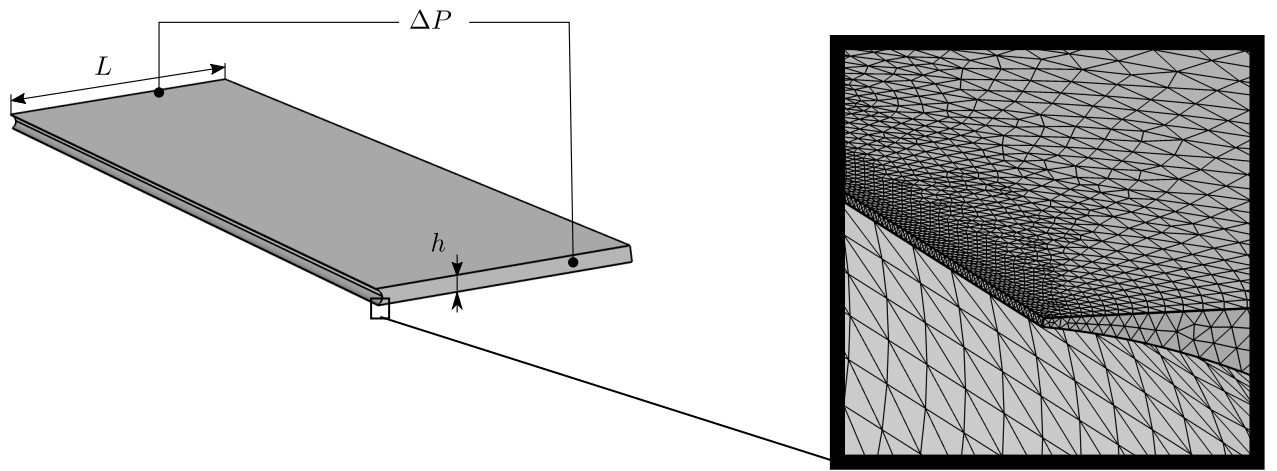


Figure 13: Microchannel with one side is a half-circle wall and the opposite side is a flat wall with  $h/L = 1/16$  (left) and mesh detail at the small chamfer build after the cylinder extrusion (right).

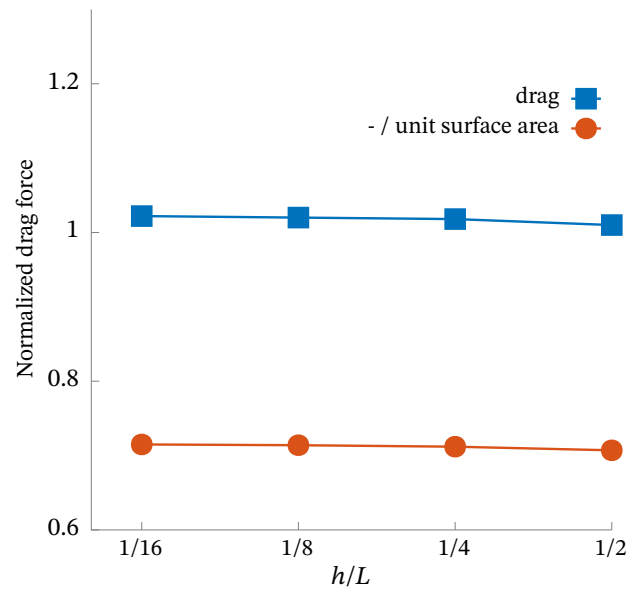


Figure 14: Drag force and drag force per unit surface area exerted upon the curved wall of the microchannel normalized with respect to the drag force exerted upon the flat wall. The drag exerted upon the curved solid wall is almost equal to the drag exerted upon the flat wall, since the smaller drag per unit surface area is almost fully compensated by the greater surface area. .

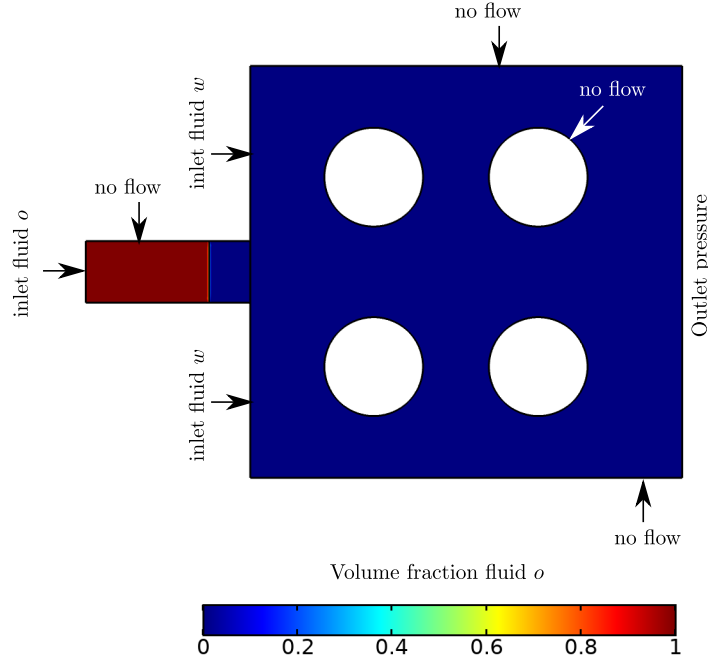


Figure 15: Test case for comparison between Level Set and Boundary Element methods. The flow is cocurrent from left to right and the viscosity is the same for both fluids.

different interfaces obtained with the LS method, depending on the initialization parameter value. This parameter is normalized with respect to the inlet velocity of fluid  $o$ , which is three times greater than the fluid  $w$  inlet velocity. One can clearly observe that the interface position obtained with the LS method is almost identical to that obtained with the BEM, regardless of value of  $\psi$ . However, the best results, especially regarding the interface tip position, is obtained for  $\psi = U_o^{\text{inlet}}$ .

### C. Calculation of the pressure part of the drag upon the fluid-fluid interface

The pressure part of the drag exerted upon the fluid-fluid boundary  $\Gamma_{ij}$  by fluid  $i$  reads

$$\int_{\Gamma_{ij}} (p_i \mathbf{I}) \cdot \mathbf{n}_{ij} d\Gamma, \quad (19)$$

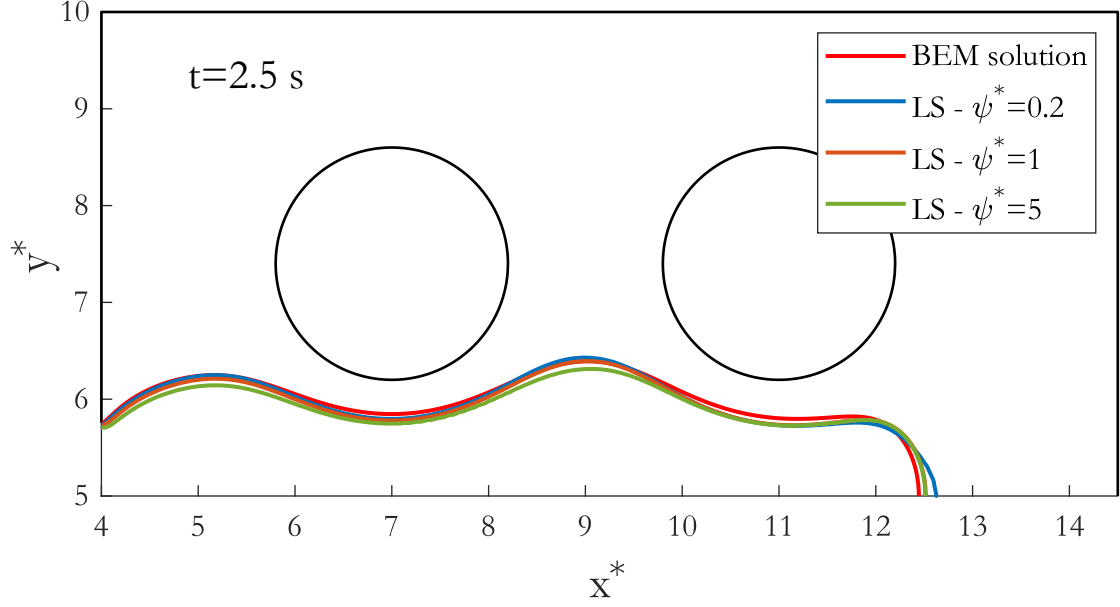


Figure 16: Interface position at time  $t = 2.5$  s obtained for an aspect ratio  $h/L = 0.25$  with a Boundary Element method and the Level Set method for different values of the dimensionless initialization parameter  $\psi^* = \psi/U_o^{\text{inlet}}$ .

where  $p_i = p_i(x, y)$ ,  $\mathbf{I}$  stands for the  $2 \times 2$  identity matrix and  $\mathbf{n}_{ij}$  is the normal unit vector at the fluid-fluid interface pointing toward fluid  $j$ . To obtain Eq. 19 we apply the divergence theorem in one unit-cell and subtract all the boundaries participation except from the fluid-fluid boundary, i.e., for fluid  $w$ ,

$$\begin{aligned} \int_{\Gamma_{wo}} \mathbf{n}_{wo} \cdot p_w \mathbf{I} \, d\Gamma &= \int_{S_w} \nabla \cdot (p_w \mathbf{I}) \, dS + \int_{\Gamma_{w-left}} p_w \mathbf{I} \cdot \mathbf{n} \, d\Gamma + \\ &+ \int_{\Gamma_{w-top}} p_w \mathbf{I} \cdot \mathbf{n} \, d\Gamma - \int_{\Gamma_{w-bot}} p_w \mathbf{I} \cdot \mathbf{n} \, d\Gamma - \int_{\Gamma_{w-right}} p_w \mathbf{I} \cdot \mathbf{n} \, d\Gamma - \int_{\Gamma_{w-cyl}} p_w \mathbf{I} \cdot \mathbf{n} \, d\Gamma, \end{aligned} \quad (20)$$

where the change of sign allows to take into account the change of orientation of the normal unit vector. Taking the  $x$ -component, the integrals on the top and bottom boundaries vanish, and regarding fluid  $o$ , the integral on the cylinder's boundary vanishes, since only fluid  $w$  is

in contact with the wedges.